Design and Control of a Hand-Held Concentric Tube Robot for Minimally Invasive Surgery

Cédric Girerd and Tania K. Morimoto

***Abstract*—Minimally invasive surgery is of high interest for interventional medicine, since the smaller incisions can lead to less pain and faster recovery for patients. The current standard-of-care involves a range of affordable, manual, hand-held rigid tools, whose limited dexterity and range of adoptable shapes can prevent access to confined spaces. In contrast, recently developed roboticized tools that can provide increased accessibility and dexterity to navigate and perform complex tasks, often come at the cost of larger, heavier, grounded devices that are teleoperated, posing a new set of challenges. In this paper, we propose a new hand-held concentric tube robot with an associated position control method that has the dexterity and precision of large roboticized devices, while maintaining the footprint of a traditional hand-held tool. The device shows human-in-the-loop control performance that meets the requirements of the targeted application, percutaneous abscess drainage. In addition, a small user study illustrates the advantage of combining rigid body motion of the device with more precise motions of the tip, thus showing the potential to bridge the gap between traditional hand-held tools and grounded robotic devices.**

I. Introduction

MINIMALLY invasive surgery (MIS) is revolutionizing medical operations by minimizing the impact of procedures on the patient [1], [2]. By entering the body through small incisions or natural orifices, the complication risk, pain and recovery time can all be decreased. However, entering the human body through small entry points and navigating tortuous paths around obstacles to reach surgical sites, requires the surgical tool to have a high degree of dexterity. To date, two main classes of devices have been proposed and used in operating rooms for MIS. On one end of the spectrum, there are traditional hand-held, rigid tools, that are typically affordable and designed for a range of procedures. However, they necessitate a direct path from their entry point to the surgical site, which is not possible in many scenarios. They can also be subject to tremors, since they are directly held by the physicians. And on the other end of the spectrum, there are a number of recently developed roboticized devices that offer higher stability, dexterity, and accessibility to the surgical site. However, these systems are usually larger and heavier master-slave devices that are grounded and teleoperated, posing a new set of challenges.

Bridging the gap between these two classes of systems are several hand-held surgical devices that offer increased dexterity compared to hand-held rigid tools, while maintaining a similar footprint and general workflow [3]. These devices are typically equipped with joints, usually located close to the tip of the instrument, that provide distal dexterity. We propose that the integration of even higher dexterity tools would further enhance the capabilities of these hand-held devices, helping to improve a number of procedures. One specific procedure that could benefit from more dexterous devices is percutaneous abscess drainage. Such abscesses form due to the release of bacteria and other substances during accute forms of appendicitis for instance, and can get perforated, thus releasing the abscess content in the abdominal cavity [4], [5]. Percutaneous abscess drainages with catheters are then performed under ultrasound or CT imaging modalities to remove the abscess liquids [4]. Reaching the target locations to fully drain all liquids while avoiding sensitive anatomy is difficult with the current tools. Yet, it is of primary concern to avoid additional complications [4], [5], and this application could benefit from more dexterous hand-held instruments.

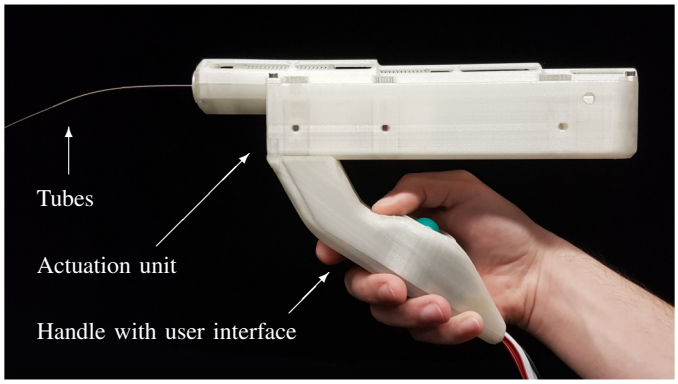

Fig. 1. Proposed hand-held concentric tube robot (CTR) with deployed tubes, actuation unit, and handle equipped with a user interface.

A. Hand-held surgical devices

Recent hand-held developments for surgical devices include non-robotic articulated devices, such as one with a wrist and an elbow [6] and one with a continuously bending distal section [7], among others [8]. Hand-held robotic devices have also been developed, with recent propositions including a device with a 2 DOF bending forcep [9], one that incorporates the da Vinci EndoWrist instruments [10], and one with a single, continuously bending segment at the tip [11]. These mechanically ungrounded, comanipulated devices offer lower-cost alternatives to traditional grounded master-slave robotic systems, while simultaneously offering increased dexterity and reduced invasivness. Also, compared to their grounded counterparts, their lack of linkages can lead to improved

This work was supported in part by National Science Foundation grant 1850400.

The authors are with the Department of Mechanical and Aerospace Engineering, University of California, San Diego, La Jolla, CA 92093 USA. e-mail: cgirerd@eng.ucsd.edu; tkmorimoto@eng.ucsd.edu.

manipulability, since the motion and orientation are not constrained. In addition, the ungrounded architecture enables these robots to utilize the inherent dexterity of the operator, and their similarity to rigid hand-held medical tools makes them attractive and easy to integrate into the surgical workflow [3], enabling shorter overall procedure times due to the minimal setup required in the operating room. Despite the numerous potential benefits of hand-held surgical devices, the integration of tools with higher dexterity and degrees of freedom (DOF) is challenging due to their inherent complexity.

B. Continuum robots

Continuum robots are a promising alternative for MIS due to their ability to snake around obstacles with their continuously bending structures [12]. Unlike serial or hyper-redundant robots, which have a finite number of links and joints, continuum robots can be viewed as robots made of an infinite number of joints and links of zero length, forming a continuously bending structure. Manual and robotic articulated endoscopes were proved to have advantages such as increased dexterity and reduced invasiveness over traditional rigid ones, with their ability to bend at the tip [8], [10]. While these allow for increased dexterity by enabling more complex paths to be followed inside the human body, the use of continuum robots has the potential to push the boundaries of surgical instruments even further forward, by extending a locally bending tip to a continuously bending body, in order to navigate complex areas.

C. Concentric tube robots

Concentric tube robots (CTRs) are a particular subclass of continuum robots [13], [14]. They are made of a telescopic assembly of precurved elastic tubes, that interact in bending and torsion to reach an equilibrium [15]. They have received great attention due to their small body size of about 1 mm of diameter [15], natural hollow shape that can be used as a passageway for surgical tools or as a suction channel [16], and ability to deploy in a follow-the-leader manner, when the backbone exactly follows the tip [17]. They have been used in a variety of applications that include hemorrhage evacuation [16], vitroretinal surgery [18], lung access [19], fetoscopic [20], transnasal [21], percutaneous intracardiac beating-heart [22] and prostate [23] surgery.

The large majority of the developed prototypes that can accommodate three fully actuated for tip position control with 6 DOF are large, heavy devices that are grounded or attached to passive arms to operate [23]. This requires a specific, predetermined setup, different than the workflow of hand-held tools. Recent efforts to enable portable CTRs include prototypes with reduced number of tubes and actuated DOF, leading to limited tip control capabilities [24], [25], [26], [27], [28], with some of them remaining too heavy to be hand-held. In addition, several user input mechanisms have been considered and evaluated for use with continuum robots, including joysticks and triggers [24], [23], haptic interfaces [29], [21], 3D mouse and gamepads [30], in combination with tip pose control algorithms, that still have practical limitations [31].

D. Contributions

The primary contribution of this paper is to present the first fully hand-held, 6 DOF CTR, visible in Fig. 1. It is lightweight, compact, has a continously bending body compared to hand-held devices currently in use in operating rooms, and is controlled with a user interface located on its handle. In addition, we present improvements and merging of several previous CTR developments. First, we propose a method for position control in the case of stable tube sets, that solves previous limitations when tube translations computed would be outside of their possible range. Second, the proposed method includes a way to efficiently compute and store the workspace boundaries of concentric tube robots, enabling a limit to be placed on the user input to stay inside the reachable workspace. Finally, the designed prototype and associated control are assessed experimentally in the case of percutaneous abscess drainage, and the accuracy, added dexterity, and usability of the system are demonstrated.

The paper is organized as follows: Section II presents background information on CTRs, necessary for the understanding of the remainder of the paper. Section III presents the design requirements, proposed design, and important characteristics of the prototype. In Section IV, we then propose a position control method for stable CTRs. The evaluation of the control method is conducted in Section V on a tube set, and the evaluation of the device performance is conducted in Section VI. Conclusions and perspectives are finally presented in Section VII.

II. Background: Concentric Tube Robot Modeling

In this section, we present background on CTR kinematics, stability, and workspace analysis, that serves as a base for the

TABLE I
NOMENCLATURE

n	Number of tubes in the CTR
i	Tube index of the CTR, numbered in increasing diameter order
κ_i	Curvature of tube i
L_i	Length of tube i from its attachment point to its tip
β_i	Transmission length of tube i
δ_{β_i}	Additional attachment length of tube i on its respective actuators
k_{ib}	Bending stiffness of tube i
k_{it}	Torsional stiffness of tube i
ψ_i	Angle between the material frame of tube i and $\mathbf{R}_B$
θ_i	Angle of tube i relatively to tube 1
$\mathbf{u}_i$	Deformed curvature vector of the i-th tube
$\mathbf{R}_i$	Rotation matrix of the Bishop frame of the i-th tube
$\mathbf{p}_i$	Position of the backbone Bishop frame of the i-th tube
s	Curvilinear abscissa of the CTR
$\mathbf{e}_i$	$i-th$ standard basis vector
$\hat{}$	Conversion of an element of $\mathbb{R}^3$ to an element of $\mathfrak{so}(3)$
$\mathbf{q}$	Complete set of kinematic inputs of the CTR
$\mathbf{q^r}$	Reduced set of kinematic inputs of the CTR
$\mathcal{P}$	Random set of 3D tip positions reached by the CTR
$\tilde{\mathbf{p}}$	Approximated CTR tip position computed from the truncated Fourier series
$\mathbf{p}_{des}$	Desired tip position of the CTR in the Cartesian space
$\mathbf{R}_z(\alpha)$	Rotation matrix of angle α about the z-axis
$\mathbf{J}$	Jacobian matrix associated to the position control
$\mathbf{J}^\dagger$	Pseudo-inverse of $\mathbf{J}$

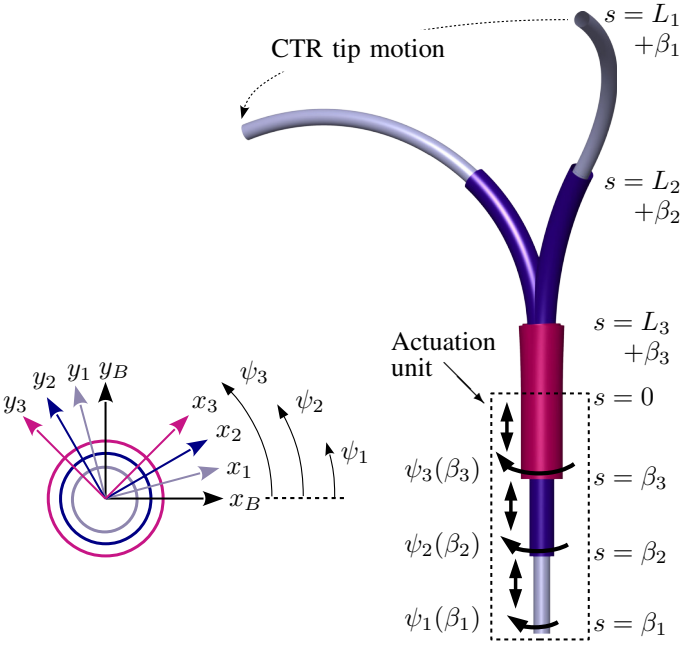

Fig. 2. On the right: illustration of a 3-tube CTR with deployed tube lengths $L_i+\beta_i$ and base angles $\psi_i(\beta_i)$. Two different configurations are represented, corresponding to different base angles of the tubes. On the left: cross-sectional view of the three overlapping tube link of the CTR, with the angle of the tubes relative to the Bishop frame.

remainder of this paper. A summary of all variables introduced in the paper is provided in Table I.

A. Kinematics

CTRs are made of a set of nested, precurved tubes that conform axially, leading to a continuum shape. The tubes are each held at their bases, and by translating and rotating with respect to each other, the shape of the free, deployed assembly can be actively modified. Each tube has therefore two independent kinematic inputs, leading to $2n$ independent kinematic inputs for a n-tube CTR. We define the joint space vector $\mathbf{q}^\intercal = \begin{bmatrix}\psi_1(\beta_1) & \cdots & \psi_n(\beta_n) & L_1+\beta_1 & \cdots & L_n+\beta_n\end{bmatrix}$ as the complete set of kinematic inputs, with $\psi_i(\beta_i)$ the angle at the base of tube i, and $L_i+\beta_i$ its deployed length.

A kinematic model of CTR that considers the effects of both bending and torsion has been derived from energy minimization or Newtonian equilibrium of forces [31], with the tubes twisting along their lengths to reach an equilibrium. The differential equations relating the angles of the tubes, ψ_i, and their derivatives with respect to the curvilinear abscissa of the robot, s, is a boundary value problem. The boundary conditions are the tube angles $\psi_i(\beta_i)$ at their proximal ends, and the tube torsion, which equals zero at the distal, free end, i.e. $\psi_i(L_i+\beta_i) = 0$. The torsion of the tubes is considered to be uniform inside the actuation unit, since its geometry constrains the tubes to be straight. This assumption leads to the boundary condition at the proximal ends of the tubes $\psi_i(0) = \psi_i(\beta_i) - \beta_i\dot{\psi}_i(0)$. Under the assumption of no friction and external loads, and in the case of planar piecewise constant-curvature tubes, the boundary value problem is governed by a set of differential algebraic equations given by Eq. (1) for each section where the tube number and tube curvature is constant [32].

$$k_{it}\ddot{\psi}_i = \frac{k_{ib}}{k_b}\sum_{j=1}^{n} k_{jb}\kappa_i\kappa_j \sin(\psi_i - \psi_j) \tag{1}$$

k_{ib}, k_{it} represent the bending and torsional stiffnesses, and $k_b = \sum_{i=1}^{n} k_{ib}$, with n the number of tubes in the considered CTR link. Ensuring continuity over the CTR sections and solving the boundary value problem leads to a solution for the tube angles, $\psi_i(s)$. The position and material orientation of each tube in 3D space can then be obtained by integration of Eq. (2) where $\mathbf{e}_3$ is the vector of the Bishop frame which is tangent to the robot backbone, and $\hat{\mathbf{u}}_i$ is the skew-symmetric matrix of $\mathbf{u}_i$, computed using the solution of Eq. (1) [32].

$$\begin{cases} \dot{\mathbf{p}}_i = \mathbf{R}_i\mathbf{e}_3 \\ \dot{\mathbf{R}}_i = \mathbf{R}_i\hat{\mathbf{u}} \end{cases} \tag{2}$$

Eq. (2) is associated with the boundary conditions of tube i, visible in Eq. (3),

$$\begin{cases} \mathbf{p}_i(0) = \mathbf{0} \\ \mathbf{R}_i(0) = \mathbf{R}_z(\psi_i(0)). \end{cases} \tag{3}$$

B. Stability

A CTR made of piecewise constant curvatures can have multiple solutions to the kinematic model [17], [33], corresponding to either stable or unstable configurations of the robot. A local stability criterion is known in the case of any number of piecewise constant curvature tubes [33]. The criterion is derived by linearization of the system of equations given by Eq. (1) around the equilibrium configurations to assess. The resulting subsystem is

$$\mathbf{K_t}\dot{\psi}(L_1+\beta_1) = \mathbf{W}_2\mathbf{K_t}\dot{\psi}(0), \tag{4}$$

where $\mathbf{K_t} = \mathrm{diag}(k_{1t}\cdots k_{nt})$. $\mathbf{W}_2$ depends on the tube curvatures, deployed and transmission lengths, and the bending and torsional stiffnesses of the tubes. A CTR is stable if $\det(\mathbf{W}_2) > 0$. The equilibrium angles to assess are the ones for which at least two tubes have opposite curvatures. As only the relative orientations of the tubes are of importance, the reduced set of n to $n-1$ angles $\theta_i = \psi_i - \psi_1, i \in [2, n]$, is usually introduced for convenience. Assuming that the tubes all have initial curvatures of the form $\kappa_i(s)^\intercal = \begin{bmatrix}\kappa_{ix}(s) & 0 & 0\end{bmatrix}$ or $\kappa_i(s)^\intercal = \begin{bmatrix}0 & \kappa_{ix}(s) & 0\end{bmatrix}$, the set of equilibrium angles to assess $\theta_e^\intercal = \begin{bmatrix}\theta_2 & \cdots & \theta_n\end{bmatrix}$ have their elements either equal to 0 or π [33].

C. Reachable workspace and workspace boundaries

The reachable workspace of a CTR is the set of the 3D tip positions that can be reached by the robot in Cartesian space. Current approaches use random sampling of the kinematic inputs $\mathbf{q}$ and compute the corresponding set $\mathcal{P} \in \mathbb{R}^3$ of tip positions of the robot using the kinematic model described in the previous section [34], [35], [36]. While the tubes can rotate freely, their translations are constrained, and the inequalities $L_n+\beta_n \leq \ldots \leq L_1+\beta_1$ and $\beta_1 \leq \ldots \leq \beta_n$ must be respected to ensure that the tubes are not more than fully covered at their

distal and proximal ends, respectively. However, due to the mechanical components that grab the tubes at their proximal ends on a portion $\delta_{\beta_i} > 0$ at the tube bases [34], the second inequality becomes, in practice, $\beta_i \leq \beta_{i+1} - \delta_{\beta_{i+1}}$. Finally, $\beta_i \in [-L_i, 0]$, constrains the base of the tubes to be in the actuation unit with a deployed length greater than or equal to zero. These inequalities are summarized in Eq. (5).

$$\begin{cases} L_n + \beta_n \leq \ldots \leq L_1 + \beta_1, \\ \beta_i \leq \beta_{i+1} + \delta_{\beta_{i+1}}, \\ \beta_i \in [-L_i, 0]\,. \end{cases} \tag{5}$$

The workspace boundaries are computed using the set of tip positions $\mathcal{P}$. In [36], the tip positions in $\mathcal{P}$ are rotated so that they all lie in the same $x - z$ half-plane, and the boundaries of the obtained planar point cloud are defined in a continuous manner using a set of arcs. In [34], [35], the set $\mathcal{P}$ is first split into slices of constant thickness along the z-axis. Then, the outer boundary of each slice is defined by a polygon linking all external points. CTR are also known to have holes in their workspace, particularly around the z-axis, that the tip cannot access. The same method is applied for these inner boundaries, with a threshold between the points and the z-axis to account for the sampling noise. The complete CTR boundaries are then defined by the limits of $\mathcal{P}$ along the z-axis, and by a set of outer and inner polygons for each slice.

III. Mechanical Design

In this section, we present the design requirements for a hand-held robot, describe the proposed design, and finally present the fabricated prototype.

A. Design requirements

As previously detailed, a general CTR requires each of its tubes to be actuated in translation and rotation. This leads to a rapidly growing number of actuators as the number of tubes increases. In this work, we set the maximum number of tubes equal to three, which is typically the maximum considered to-date in CTR prototypes [31]. As the device is hand-held, it should also be reasonably compact and lightweight to be used for standard surgical operations without causing the operator fatigue or pain. The operator should also be able to easily assemble and attach tubes onto the system, since the set of tubes will depend on the specific patient or task to perform.

B. Method

In order to achieve a compact lightweight system that is easy to assemble, we propose to limit the number of parts in the device by designing parts that provide multiple functionalities. Roller gears, for instance, have teeth along two orthogonal directions, enabling simultaneous rotation and translation of a tube with a single component. An initial roller gear design has been proposed for truss manipulation [37], however, the design requires a single gear to be connected to the truss at a time, necessitating the use of additional actuators to engage/disengage the rotation or translation gears. This requirement leads to an increase in the size and weight of the overall system and prevents simultaneous translation and rotation required for CTRs. We instead build upon our previous design [38], which allows simultaneous motions. Additive

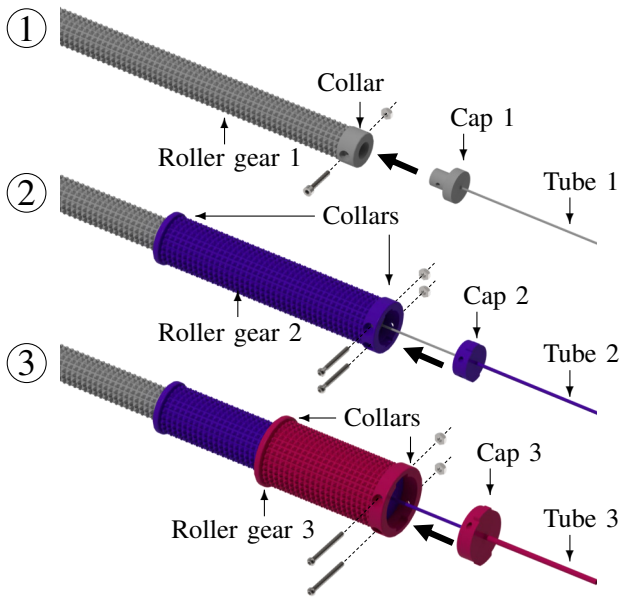

Fig. 3. Sequence of assembly steps (labeled from 1 to 3) for the attachment of the tubes, which are pre-assembled on their respective caps, to the roller gears. The final assembly is then inserted in the lower guide and covered by the upper guide as illustrated in Fig. 4.

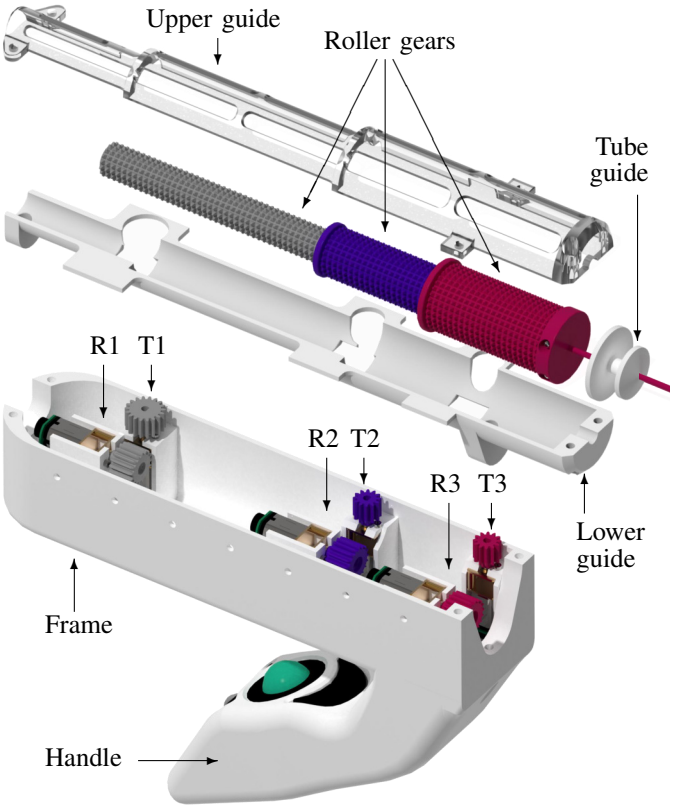

Fig. 4. Exploded view of the proposed hand-held CTR, with its main components. R1, R2, R3, T1, T2, and T3 designate the actuator and associated gear for the rotation and translation of tube 1, 2 and 3, respectively.

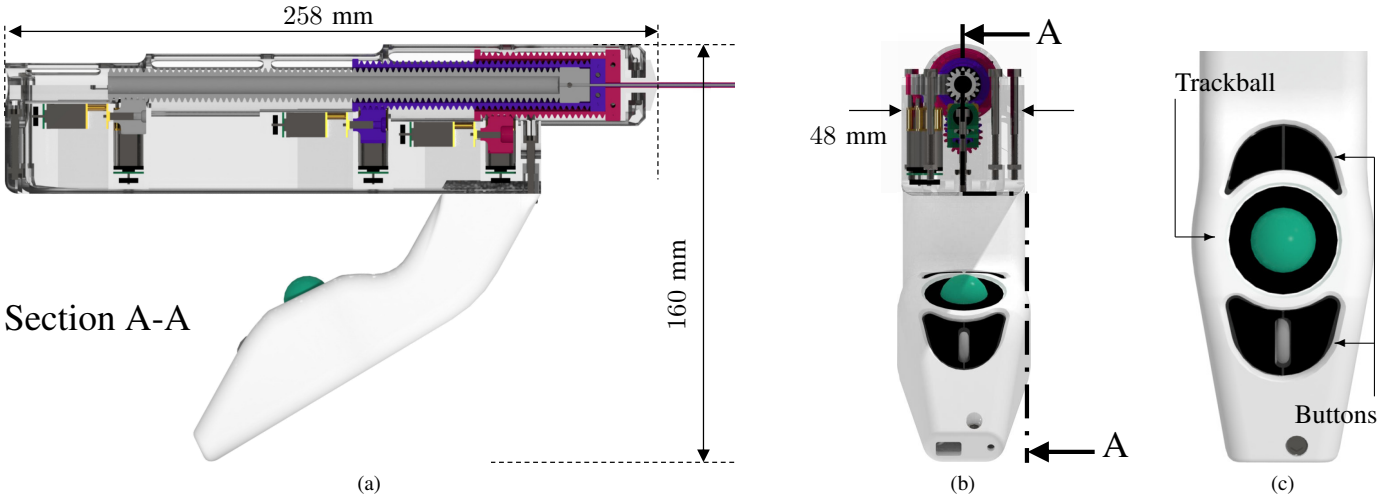

(a) (b) (c)

Fig. 5. (a) Cross-sectional and (b) back view of the prototype with its dimensions depicted, and (c) close-up view of the handle, including the user inputs. The frame and guides (upper and lower) are shown as transparent to enable visualization of the internal components.

manufacturing is used to produce the entire system in order to meet the weight requirements, which allows the production of complex parts with a lightweight material.

C. Proposed design

The device is composed of a single frame that holds all the components of the system. All actuators are attached to it, as visible in Fig. 4, where all rotation, translation and roller gears that engage together are represented with the same color for ease of understanding. The frame hosts lower and upper guides, that ensure proper movement of the roller gears during their rotations and translations (Fig. 4). To ensure this functionality, the guides have a cylindrical shape that allows the roller gears to slide inside. The roller gears are equipped with collars at their ends that contact the guides (see Fig. 3), to prevent the teeth, which are more delicate, from experiencing contact with any other part. The inner roller gear is an exception, since guiding it through its entire length would require a longer frame, leading to an increase of the device dimensions and weight. The length of a roller gear and the length of its matching section on the lower and upper guides define its stroke, and thus the stroke of the tube it holds. The stroke of each roller gear for the proposed system is reported in Table II and can be adjusted during the design depending on application requirements.

TABLE II
SPECIFICATIONS OF THE GEARS SELECTED FOR THE DESIGNED PROTOTYPE

	Module number	Gear	Teeth number	Stroke (mm)	Gear Modulus
Rotation Modules	1	Roller gear	16	∞	0.75
		Rotation gear	17		
	2	Roller gear	24	∞	
		Rotation gear	18		
	3	Roller gear	33	∞	
		Rotation gear	19		
Translation Modules	1	Roller gear	21	160	0.75
		Translation gear	18		
	2	Roller gear	39	80	
		Translation gear	12		
	3	Roller gear	76	30	
		Translation gear	12		

To enable easy tube replacement in the actuation unit, the rotation gears are placed under the roller gears, and the translation gears are placed on their sides (see Fig. 4). This feature allows access to the roller gears from the top of the device, by removing the upper guide, as illustrated in Fig. 4. The roller gears can then be removed, and other tubes can be attached to them. Additional sets of roller gears with tubes already attached can also be directly inserted into the device. Concentric assembly of the roller gears, with the tubes attached, is shown in Fig. 3. Tubes are initially glued with cyanoacrylate to their respective 3D-printed caps, to avoid any constraints at the attachment locations that could lead to deformations of the tubes. These subsets are then assembled sequentially with their respective roller gears (see provided video for details on the full device assembly). We note that the proximal ends of the tubes are located inside their caps and thus do not run through the entire length of their respective roller gears.

The rotation, translation, and roller gears are produced with a PolyJet Technology, using a Connex 350 (Stratasys, USA) and VeroClear material. The Connex printer has x and y resolutions of 42 μm along the build surface, and a resolution of 16 μm along the vertical z axis. These resolutions are orders of magnitude smaller than characteristic dimensions of the features to print, with teeth height of about 1.7 mm for comparison, and ensures a proper quality for these parts. The other parts were produced with PLA using a Ultimaker 3 FDM printer (Ultimaker, Netherlands). Six Pololu (Las Vegas, USA) 298:1 Micro Metal Gearmotor HPCB 12V with extended motor shafts are selected for the actuation of the roller gears. Each of them is equipped with a quadrature encoder mounted on the extended shaft of the motor. This set of 6 motors equipped with encoders are connected to 6 Faulhaber MCDC

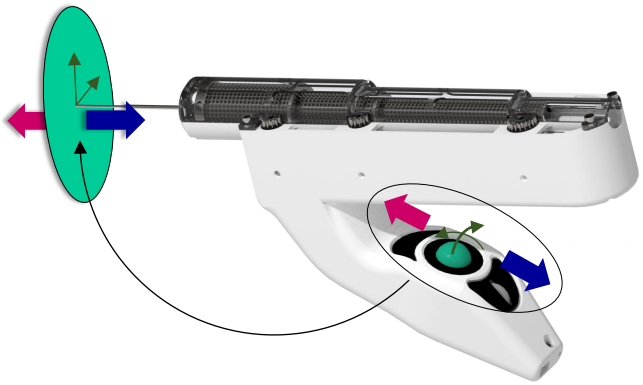

Fig. 6. Mapping between the inputs on the handle and the motions of the CTR tip in Cartesian space.

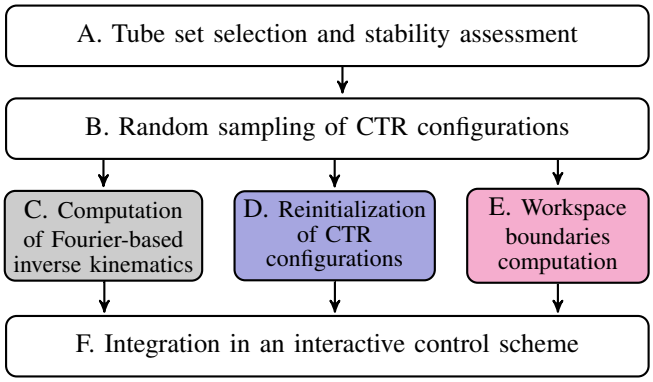

Fig. 7. Flowchart showing the different steps of the proposed control method.

3006 S RS motor controllers (Faulhaber, Germany) with cable ribbons, consisting of 6 wires. They are connected to the host computer with USB cables, and are powered with a 12 V DC power supply. The overall weight of the prototype is 370 g with all 6 motors representing a total of 100 g, for a length, height and width of 258, 160 and 48 mm, respectively, as depicted in Fig. 5. It should be noted that the overall length of the device can be larger, since the back of the inner roller gear can extend further from the back of the frame of the actuation unit. In the worst case scenario when the inner roller gear is fully retracted, the total length would be 382 mm. The overall length highly depends on the lengths and stroke of the tubes that will be manipulated, and varies during deployment.

D. Handle and user interface mapping

The handle of the device is designed to enable single-hand operation. All user inputs have a vertical symmetry, allowing it to be used indiscriminately by right-handed and left-handed persons, compared to devices that do not present such symmetry [24]. The handle is equipped with a trackball, located between two buttons, as shown in Fig. 6, and is connected to a computer using a USB cable. An intuitive mapping between the user interface and the motions of the robot's tip is thus proposed as follows. Pressing the button in the front leads to the tip of the robot moving forward, while pressing the button in the back leads to the tip of the robot moving backward. This mapping is coherent with the spatial layout and corresponding tip motion directions. The trackball, located between these buttons, does not lead to deployment of the CTR tip, but instead enables the user to control in-plane motions, as visible in Fig. 6.

IV. Position Control Method

In this section, we present a method for the position control of a CTR tip in 3-D space, for concentric tube robots that are stable and not subject to external loads. It allows for 3-DOF control of a CTR tip along the x, y and z axis in Cartesian space. Prior work on the position and orientation control of CTRs includes a partially offline method that makes use of multi-dimensional Fourier series with a root finding method to solve for the inverse kinematics [15], [39]. In the absence of CTR instabilities and external loads, this is the most time-efficient approach compared to other approaches that use Jacobian and compliance matrices in [40] or modified Jacobian-based approaches with torque sensors [41], as detailed in [31]. In addition, the solving speed of the multi-dimensional Fourier series is consistent, with the inverse kinematics running at a frequency of 1000 KHz [15], [39], making it suitable for interactive or real-time control. Finally, another advantage of this partially offline method is the ability to identify numerical problems of the inverse kinematics offline, offering greater reliability during the CTR usage [31]. This approach is thus used as a base in our developments.

There remain limitations that influence the effectiveness and practical use of this partially offline approach. First, the use of a truncated Fourier-based approach requires a stable CTR, as detailed in [31], which was not previously assessed in the original approaches. Second, the multi-dimensional Fourier series is based on initial random CTR configurations that are feasible, in the sense that they respect Eq. (5). However, the associated root finding method treats each joint value independently during convergence, potentially resulting in solutions to the inverse kinematics that may not satisfy Eq. (5). These solutions could lead to critical issues, including unexpected CTR geometries if tubes are more than fully covered at their distal ends, or collisions in the actuation system if they are more than fully covered at their proximal ends. Finally, no approach to date has considered limiting the user inputs to the reachable robot workspace.

We propose a method for the position control of CTRs that addresses these limitations, by (1) assessing the CTR stability before implementing the inverse kinematics, (2) reinitializing CTR configurations that are not feasible, and (3) providing a new way to compute and store the workspace boundaries that seamlessly integrates into our workflow and is time-efficient. The latter allows us to effectively limit the user inputs during CTR usage. The steps of the proposed method are visible in the Fig. 7.

A. Tube set selection and stability assessment

The first step of the proposed method is to select a tube set. This is usually performed based on the surgical task requirements and the patient's anatomy. Then, the CTR stability must

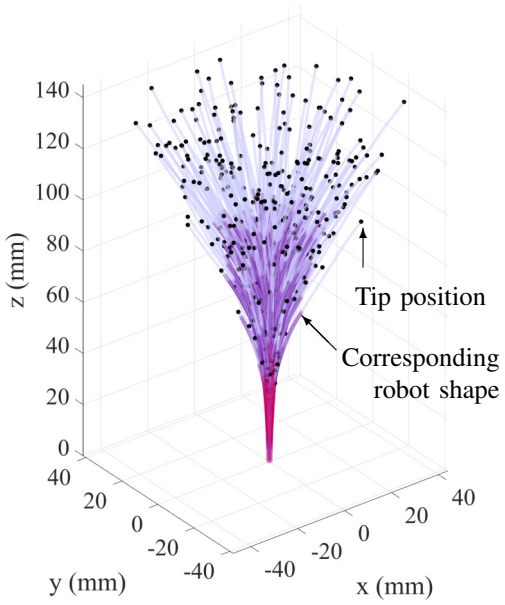

Fig. 8. Illustration of a set of random CTR configurations, with the tubes of each configuration represented in magenta, violet and grey, and the corresponding tip positions highlighted in black.

be assessed. To do this, $\det(\mathbf{W}_2)$, introduced in Section II, is computed on a grid of feasible tube translations, as given by Eq. 5, for each equilibrium angles $\theta_e^\intercal$. The considered CTR is stable if $\det(\mathbf{W}_2) > 0$ for each configuration.

B. Random sampling of CTR configurations

The second step of our method consists of generating a set $\mathcal{P}$ of random CTR configurations that respect the conditions stated in Eq. (5). Fig. 8 illustrates the random CTR configurations obtained, along with their corresponding tip positions. As rotation of all the tubes produces rigid body motion, the kinematic inputs $\mathbf{q}$ can be reduced by one rotational component. The inner tube of the CTR is considered to have a fixed orientation, and a reduced set of kinematic inputs, $\mathbf{q^r} = [\theta_2(\beta_2), \cdots, \theta_n(\beta_n), L_1 + \beta_1, \cdots, L_n + \beta_n]$, is used to generate the random configurations.

C. Computation of Fourier-based inverse kinematics

The set $\mathcal{P}$ of random CTR configurations is approximated by products of truncated Fourier series of order k for each 3D tip coordinate (x, y, z), as detailed in [15], [39]. This approximates tip positions $\mathbf{p} = [x, y, z]$ by an analytical expression $\tilde{\mathbf{p}}(\mathbf{q^r})$, which relates the coordinates of the CTR tip to the reduced set of kinematic inputs $\mathbf{q^r}$, as given by Eq. (6):

$$\tilde{\mathbf{p}}(\mathbf{q^r}) = \begin{bmatrix} f_x(\mathbf{q^r}) \\ f_y(\mathbf{q^r}) \\ f_z(\mathbf{q^r}) \end{bmatrix}, \tag{6}$$

with functions $f_x(\mathbf{q^r})$, $f_y(\mathbf{q^r})$, and $f_z(\mathbf{q^r})$ of the form:

$$f_{x,y,z}(\mathbf{q^r}) = \prod_{i=1}^{2n-1} H(\mathbf{q^r}_i/\lambda_i, k), \tag{7}$$

where $H(x, k)$ is a truncated Fourier series of order k of the form

$$H(x, k) = \sum_{j=-k}^{+k} c_j e^{i(jx)}. \tag{8}$$

λ_i is the wave scaling factor of the reduced set of kinematic inputs [15], [39]. The coefficients c_j are computed using a least square method on the set $\mathcal{P}$. The estimated tip position as a function of the complete kinematic inputs, $\tilde{\mathbf{p}}(\mathbf{q})$, is obtained using

$$\tilde{\mathbf{p}}(\mathbf{q}) = \mathbf{R}_z(\psi_1)\tilde{\mathbf{p}}(\mathbf{q^r}), \tag{9}$$

where $\mathbf{R}_z(\psi_1)$ is the rotation matrix of angle ψ_1 about the z-axis. The inverse kinematics is then solved by an implementation of the Newton-Raphson algorithm as given by

$$\mathbf{q}_{k+1} = \mathbf{q}_k - \gamma \mathbf{J}^\dagger \mathbf{F}(\mathbf{q}_k), \tag{10}$$

with

$$\mathbf{F} = \tilde{\mathbf{p}}(\mathbf{q}_k) - \mathbf{p}_{des} \quad \text{and} \quad \mathbf{J} = \frac{\partial \mathbf{F}}{\partial \mathbf{q}}, \tag{11}$$

where $\mathbf{p}_{des}$ is the desired tip position given by the user, and $\mathbf{F}$ is the difference between the computed tip position at step k and the desired one, and for which a zero must be found. $\mathbf{J}^\dagger$ denotes the pseudo-inverse of $\mathbf{J}$, which is used due to the presence of redundancies for tip position control in the 3D space if the number of actuators in the system is greater than 3, and $\gamma \in [0, 1]$ is a coefficient that controls the step size of each iteration of the Newton-Raphson algorithm.

D. Reinitialization of CTR configurations

Infeasible CTR configurations obtained by the root finding method are detected by verification of Eq. (5) for each obtained solution. In cases where Eq. (5) is not satisfied, the initial set of feasible CTR configurations $\mathcal{P}$ is used to reinitialize the CTR. First, a subset of candidate CTR configurations $\mathcal{P}_c$ for the reinitialization are extracted from the set $\mathcal{P}$, such that

$$\begin{aligned} \mathcal{P}_c : \{\mathbf{p}_c \in \mathcal{P} \quad | \quad & \|(\mathbf{p}_c - \mathbf{p}_{des}) \cdot \mathbf{e}_z\| \leq \epsilon_z \quad \text{and} \\ & \text{abs}(\|\mathbf{p}_c \wedge \mathbf{e}_z\| - \|\mathbf{p}_{des} \wedge \mathbf{e}_z\|) \leq \epsilon_r\}. \end{aligned} \tag{12}$$

The first condition ensures that the tip of the candidate configurations and the desired tip position have close z-components (with a tolerance of ϵ_z), while the second condition ensures that their radial distances to the z-axis are close (with a tolerance of ϵ_r) This is illustrated in Fig. 9 (a), with an infeasible CTR configuration represented in red and 10 reinitialization candidates. Rotation of the entire CTR bodies (i.e., of all its component tubes) are applied for their tips to be radially aligned with the desired one, as visible in Fig. 9 (b). Finally, a reinitialization configuration is selected among this set, that satisfies a desired criterion. In this work, we choose to select the candidate that minimizes the total angular displacement of the motors required to reach it from the current configuration, allowing a quick reinitialization as well as a limited motion

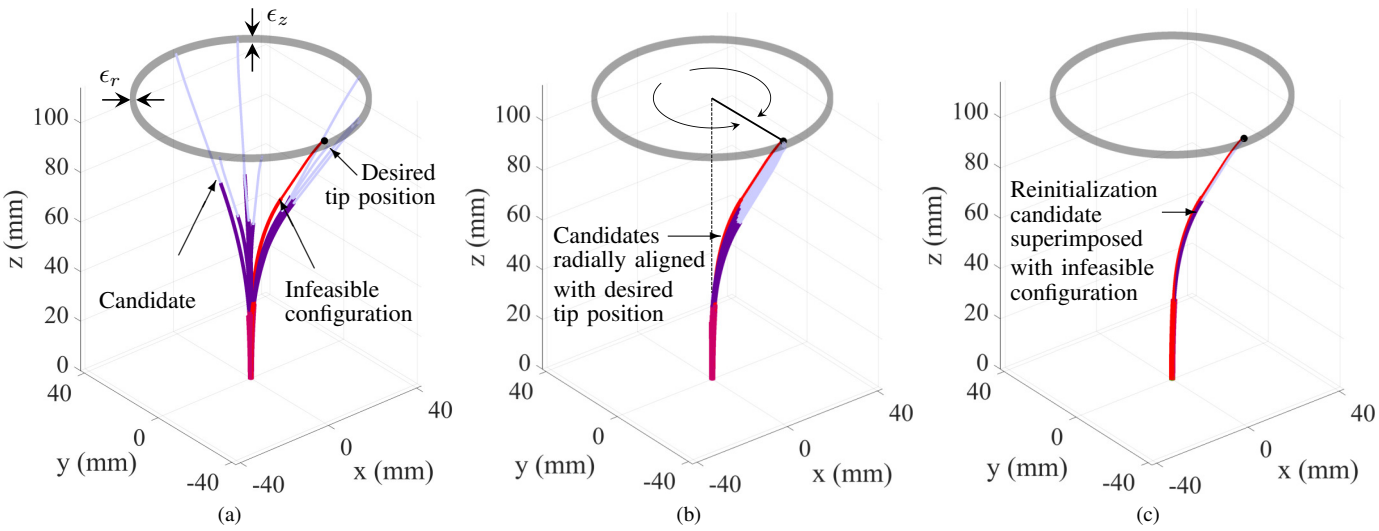

Fig. 9. Illustration of the search for a reference configuration in the case of 10 candidates in three steps: (a) identification of reinitialization candidates, (b) radial alignment of the reinitialization candidates' tip with the desired tip position, and (c) selection of reinitialization configuration.

of the CTR body. Fig. 9 (c) shows the selected configuration for the reinitialization, as well as the infeasible configuration given by the inverse kinematics.

E. Workspace boundaries computation

During interactive control of the device, it is required to limit the user input by checking if the desired tip position is in the reachable workspace. While current approaches to compute CTR workspace boundaries use random sampling of all kinematic inputs $\mathbf{q}$, we propose to use the reduced set of kinematic inputs $\mathbf{q^r}$. This approach allows for a seamless integration of the workspace boundaries computation with our control method represented in Fig. 7. Since a random set of CTR configurations based on $\mathbf{q^r}$ is already computed for the identification of the Fourier series coefficients and reinitialization configurations, it is therefore reused for the workspace boundaries computation. Also, an additional benefit of the proposed approach is its time efficiency compared to previous ones that rely on the complete set of kinematic inputs $\mathbf{q}$ (see Section II for details on these approaches). To achieve this, we take into account the fact that a rotation of all the tubes produces rigid body motion, leading to a workspace that has a cylindrical revolution about the z-axis. The workspace boundaries can then be defined as a set of circles that contain a dense and continuous set of points in a given slice along the z-axis. The computation of the workspace boundaries is performed as follows. First, the boundaries of the workspace along the z-axis are determined, with upper and lower limits z_{min} and z_{max}, respectively, such that

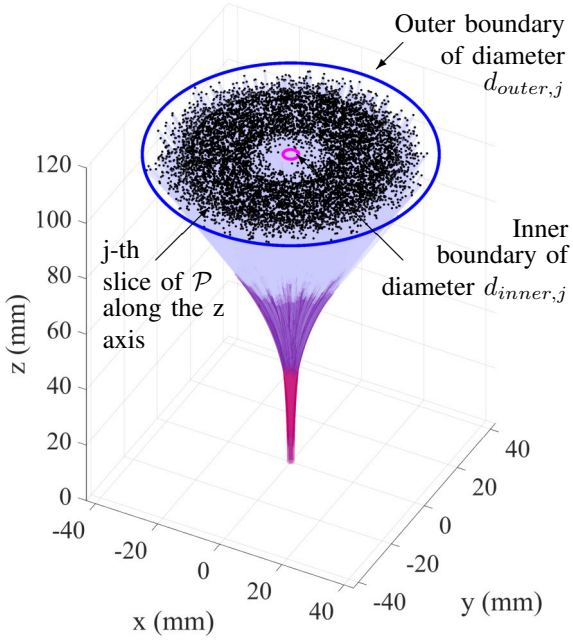

Fig. 10. Illustration of the workspace boundaries for the j-th slice of a CTR's workspace, with the inner boundary of diameter $d_{inner,j}$ in magenta and the outer boundary of diameter $d_{outer,j}$ in blue.

$$z_{max} = \max_{\mathcal{P}}(\mathbf{p}\cdot\mathbf{e}_z), \quad z_{min} = \min_{\mathcal{P}}(\mathbf{p}\cdot\mathbf{e}_z). \tag{13}$$

The set $\mathcal{P}$ is separated in l slices of thickness h along the z-axis, and we define the subsets $\mathcal{P}_{j,j\in[0,l-1]}$ such that

$$\mathcal{P}_{j,j\in[0,l-1]} : \{\mathbf{p}\in\mathcal{P} \quad | \quad jh \leq \mathbf{p}\cdot\mathbf{e}_z \leq (j+1)h\}. \tag{14}$$

The boundaries for each slice are then defined by an inner and outer circle of diameter $d_{outer,j}$ and $d_{inner,j}$, respectively, as illustrated in Fig. 10. They are located in the middle of each slice, with a threshold d_{min} considered for $d_{inner,j}$ in order to account for the sampling noise, such that

$$d_{outer,j} = \max_{\mathcal{P}_j}(\|\mathbf{p}\wedge\mathbf{e}_z\|) \tag{15}$$

$$d_{inner,j} = \begin{cases} \min\limits_{\mathcal{P}_j}(\|\mathbf{p}\wedge\mathbf{e}_z\|) & \text{if} \quad \min\limits_{\mathcal{P}_j}(\|\mathbf{p}\wedge\mathbf{e}_z\|) > d_{min} \\ 0 & \text{otherwise} \end{cases} \tag{16}$$

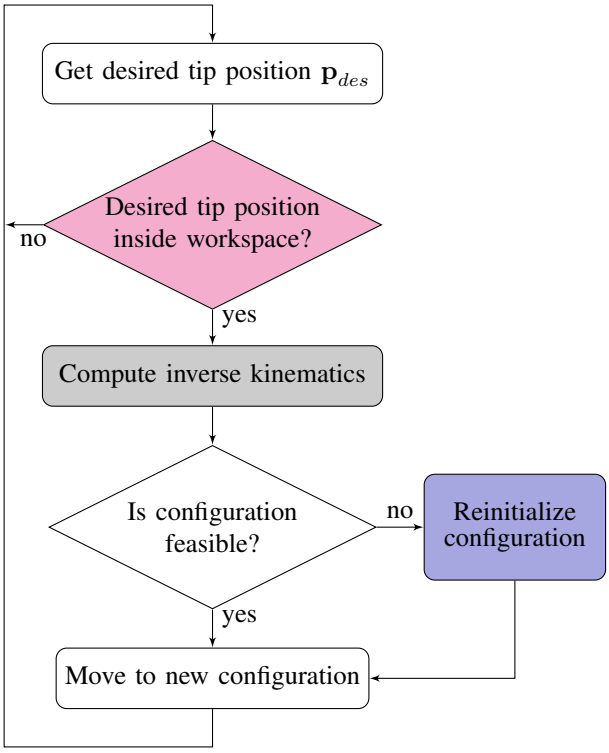

Fig. 11. Implementation of the interactive tip position control of the hand-held device.

The entire boundary of the CTR is then determined by z_{max}, z_{min}, $d_{outer,j}$ and $d_{inner,j}$.

F. Integration in an interactive control scheme

Finally, the multi-dimensional Fourier-based inverse kinematics, reinitialization using reference configurations, and computation of the workspace boundaries are combined in a control scheme, that allows the interactive tip position control of the CTR by a user. The first step consists of the acquisition of the desired tip position $\mathbf{p}_{des}$ from the user interface. If $\mathbf{p}_{des}$ is inside the reachable workspace of the robot, a solution to the inverse kinematics is computed. If the obtained solution to the inverse kinematics is feasible, i.e. if it satisfies Eq. (5), the CTR actuators are moved to the corresponding joint values. If it does not satisfy Eq. (5), the CTR configuration is reinitialized, and the CTR actuators are moved to the joint values that correspond to the ones of the reinitialized configuration. The control scheme is visible in Fig. 11.

V. Evaluation: Control Method

In order to validate the control approach, the method presented in Fig. 7 is followed using an example tube set, with the details of each step, and evaluation of the overall control performance.

A. Tube set selection and stability assessment

We use a set of three tubes to assess the performance of our system. The constraints for the selection of a tube set are that their lengths should be compatible with the stroke allowed by the roller gears, and that they should conform to make a stable robot. The designed actuation unit allows maximum tube strokes of 160 mm, 80 mm and 30 mm for tube 1 to 3 (see Section III). For the purpose of this evaluation, and without loss of generality, we select maximum deployed lengths for tube 1, 2 and 3 of 150 mm, 100 mm and 50 mm, respectively. The tubes consist of a straight section followed by a constant-curvature section, with curvatures and other important parameters reported in Table III. These parameters lead to a minimum deployed length of 20 mm for the tubes, acceptable for the targeted application, as the surgeon can insert the first few millimeters by manually moving the entire device. The next step to validate the proposed tube set is to assess its stability, using the stability criterion developed in the literature and presented in Section II, with the condition of $\det(\mathbf{W}_2) > 0$. Since a local stability criterion is used, it is evaluated on a grid of deployed lengths with $20 \leq L_1 \leq 150$ mm, $20 \leq L_2 \leq 100$ mm and $20 \leq L_3 \leq 50$ mm, with a step size of 1 mm. All equilibrium angles, which correspond to tube base angles for which at least two tubes have opposite overlapping curvatures, must be assessed to determine the stability state over the entire workspace. The equilibrium configurations to assess thus depend on the deployed lengths considered, and all different cases are summarized in Eq. (17).

$$\theta_e^{\intercal} = \begin{cases} \begin{bmatrix} 0 & \pi \end{bmatrix} & \text{if } (L_1+\beta_1)-(L_3+\beta_3) < 15 \\ & \text{or } (L_2+\beta_2)-(L_3+\beta_3) < 50 \\ \begin{bmatrix} \pi & 0 \end{bmatrix} & \text{if } (L_1+\beta_1)-(L_2+\beta_2) < 15 \\ & \text{or } (L_2+\beta_2)-(L_3+\beta_3) < 50 \\ \begin{bmatrix} \pi & \pi \end{bmatrix} & \text{if } (L_1+\beta_1)-(L_2+\beta_2) < 15 \\ & \text{or } (L_1+\beta_1)-(L_3+\beta_3) < 15 \end{cases} \tag{17}$$

For the set of tubes proposed in Table III, the minimum of $\det(\mathbf{W}_2)$ is obtained for the equilibrium $\theta_e^{\intercal} = \begin{bmatrix} \pi & \pi \end{bmatrix}$, and equals 0.72, which is greater than 0. The CTR is thus stable over its entire workspace, and can be controlled everywhere within it using the method detailed in Section IV.

B. Random sampling of CTR configurations

A set $\mathcal{P}$ of 1 million tip positions corresponding to random CTR configurations is generated with the reduced set of kinematic inputs $\mathbf{q}^{\mathbf{r}}$. Parallel computation is used to speed up

TABLE III
Tube set parameters

Parameter	Value		
Tube Index	1	2	3
Young Modulus (GPa)	80	80	80
Poisson's Ratio	0.33	0.33	0.33
Inner Diameter (mm)	0.650	1.076	1.470
Outer Diameter (mm)	0.880	1.296	2.180
Straight Section Length (mm)	162	65	15
Curved Section Length (mm)	15	50	50
Curved Section Curvature (mm^{-1})	0.0061	0.0133	0.0021

this process. The computation time was 1 hour and 15 minutes on an Intel Core i7-8700K Processor, with 16 GB of RAM. The obtained set $\mathcal{P}$ is visible in Fig. 14.

C. Computation of Fourier-based inverse kinematics

Each component x, y and z of $\mathcal{P}$ is approximated by a product of Fourier series of order 2 for each component of $\mathbf{q^r}$, leading to 3125 Fourier coefficients to identify for each component. The relationship $\lambda_j = 2\pi/max(L_j + \beta_j)$ is used to scale the deployed lengths of the tubes (see Eq. (7)). The Fourier coefficients are estimated using a least squares method on $\mathcal{P}$. For computation tractability, a subset of 75000 tip positions from $\mathcal{P}$ is used. The RMS error on the tip position with this functional approximation on the set of 75000 tip positions is 0.15 mm, with a maximum of 1.24 mm. After identification of the Fourier coefficients, the RMS and maximum errors are computed for all points of $\mathcal{P}$. They equal 0.16 mm and 2.61 mm, respectively. These errors remain low and validate the proposed approach.

Fig 12 is a representation of the set $\mathcal{P}$ with colors corresponding to the position error. As visible in this figure, the errors on the CTR workspace are not distributed uniformly. To understand this spatial distribution, Fig. 13 illustrates histograms that represent the repartition of the values of $\mathbf{q^r}$, used for the computation of Fourier series (i.e. $L_i + \beta_i$ (deployed tube lengths) and $\theta_i(\beta_i)$ (tube base angles)), for points of $\mathcal{P}$ that have a position error estimation higher that 0.3 mm. It is visible that the number of tip error occurrences is increasing for minimum and maximum deployed tube lengths, i.e. 20 and 150 mm for tube 1 (Fig 13 (a)), 20 and 100 mm for tube 2 (Fig 13 (b)), and 20 and 50 mm for tube 3 (Fig 13 (c)). This is due to the fact that the deployed lengths of the tubes have a discontinuous contribution on the CTR tip position at their minimum and maximum deployed lengths in the Fourier series, i.e. every $2k\pi, k \in \mathbb{Z}$, after scaling with the factor $\lambda_j = 2\pi/max(L_j + \beta_j)$. These discontinuities lead to fitting errors at their minimum and maximum deployed lengths, leading to errors in the CTR tip position estimation. A high number of occurrences can also be observed for deployed tube lengths of 100 mm for tube 1 and 50 mm for tube 2,

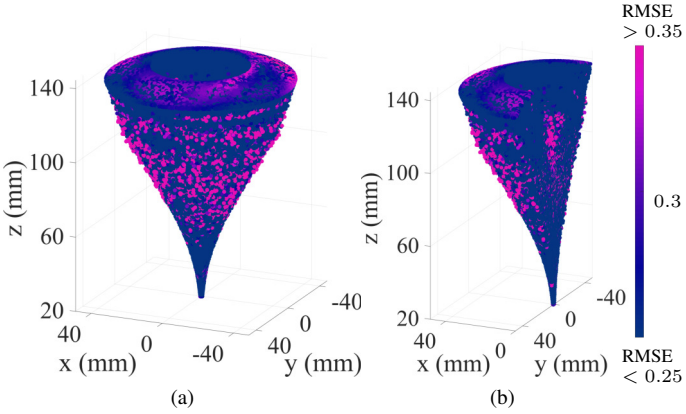

Fig. 12. Accuracy of the functional approximation of the workspace by Fourier series depending on tip position, with (a) perspective view and (b) cut view along the x axis.

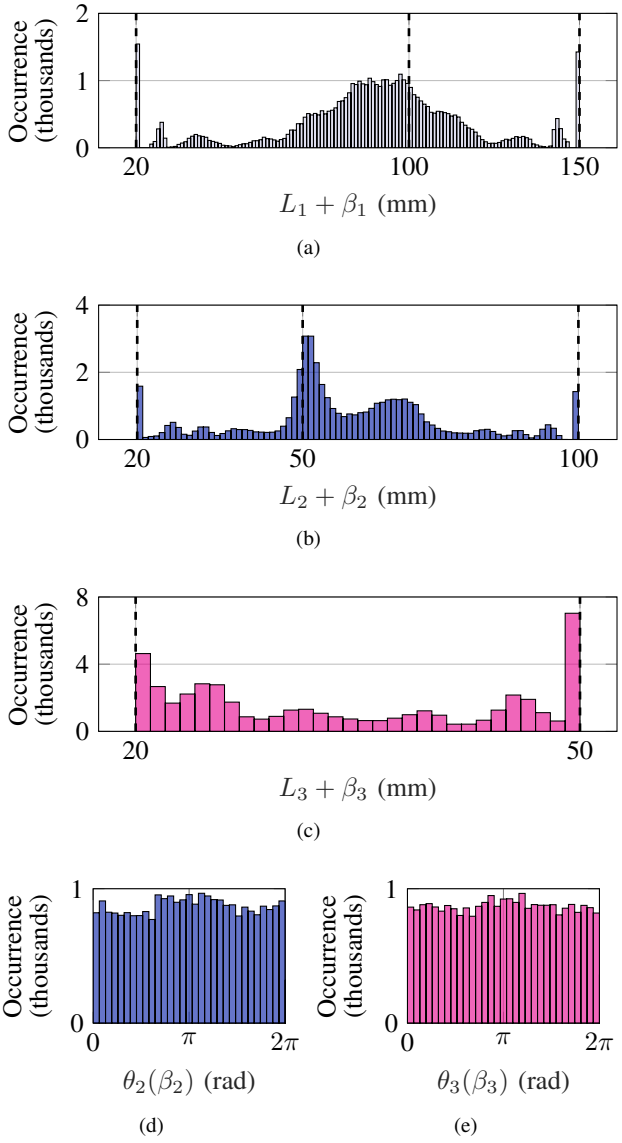

Fig. 13. Histograms showing the distribution of $L_i + \beta_i$ (deployed length of tube i) and $\theta_i(\beta_i)$ (base angle of tube i relatively to tube 1) for all points of $\mathcal{P}$ that have a position error greater than 0.3 mm.

which represent errors of tubes of smaller diameters that reach their maximum deployed length. This effect does not exist for the tube angles, which have a continuous contribution on the CTR tip position as they are rotated, as visible in Fig 13 (d) and 13 (e).

D. Reinitialization of CTR configurations

The entire dataset $\mathcal{P}$ is used for reinitialization of the CTR configurations. In order to speed up the search for candidate configurations, $\mathcal{P}$ is sorted in increasing order of the z-component of the tip position. This allows to efficiently obtain indexes in $\mathcal{P}$ that correspond to a given slice along the z-axis.

E. Workspace boundaries computation

The workspace boundaries are computed using $\mathcal{P}$ for slice thicknesses $h = 1$ mm along the z-axis and $d_{min} = 1$ mm.

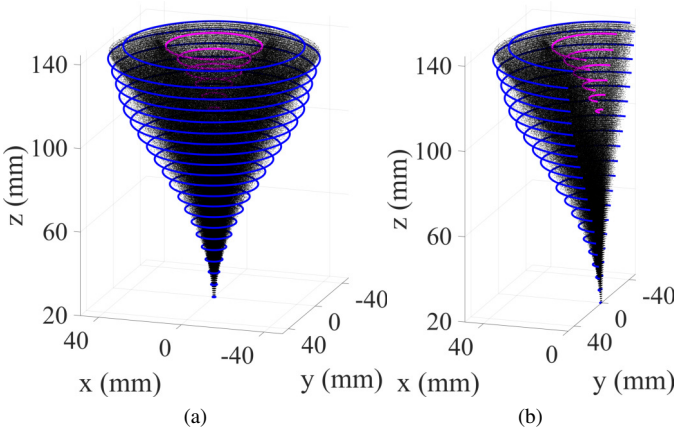

Fig. 14. Illustration of point cloud $\mathcal{P}$ with the inner and outer boundaries of the workspace in magenta and blue, respectively. Boundaries are represented every 6 mm for each of visualization.

Computed inner and outer boundaries are visible in Fig. 14, with the inner boundaries represented in magenta and the outer boundaries represented in blue. Both boundaries of a given slice along the z-axis delimit the point cloud visible in black, that correspond to random CTR tip positions of $\mathcal{P}$.

F. Integration in an interactive control scheme

Finally, the control scheme presented in Fig. 11 is implemented in Matlab (The Mathworks, Inc, USA). A value of 0.5 for γ was determined experimentally (see Eq. (10)), and allows for a convergence of the Newton-Raphson algorithm in a minimum number of steps during normal device usage, with average displacement speeds of the tip. With this implementation, the Fourier-based inverse kinematics algorithm converges in less than 3 iterations, with an average computation time of 1.2 ms for each iteration. The search for a reinitialization configuration, when necessary, takes 2.5 ms on average suitable for interactive control. Each button press is mapped to an incremental tip displacement of 0.5 mm along the z-axis. One full trackball revolution is mapped to a tip displacement of 80 mm in the xy plane, such that the CTR tip will cross the workspace diameter, at its largest location along the z-axis, with approximately one trackball revolution (see Fig. 14). This mapping results in a resolution of 0.1 mm in Cartesian space.

VI. Evaluation: Device Performance

In this section, the backlash in the device is first measured, and corresponding tip position error estimated. Experimental evaluations are then conducted to assess the performance of the prototype in terms of positioning accuracy, in an open-loop and human-in-the-loop control scheme. General usability and added dexterity are also assessed through a user study to measure the impact and advantages of a hand-held device for operators.

A. Impact of backlash in the device

Manufacturing tolerances, fabrication errors, and backlash in the motor gearbox and 3-D printed gears in the device can lead to tip position errors. In order to estimate this error, we conducted experiments to measure the extreme positions of each roller gear in translation and rotation, with fixed motor positions, thus taking into account errors accumulated in the entire kinematic chains. The experimental setups are visible in Fig. 15(a) and (b) respectively, in the case of roller gear 3. A plastic beam is rigidly attached to each roller gear, and positions at its limits are measured with a dial indicator as it is manually translated and rotated. Each translation and rotation measurement is repeated 10 times for each roller gear, and mean translation and angular displacements are reported in Table IV, along with their standard deviation. In order to estimate the effects of the backlash on the tip position, the backlash is then modeled as uniform random distributions centered on 0, with upper and lower bounds equal to plus and minus half the mean errors measured, respectively. We generate 100 random CTR configurations, and inject 1000 random translation and rotation errors for each. The RMS tip position error obtained for the overall set of 100000 CTR configurations assessed is 0.39 mm, with a maximum value of 1.75 mm. The combination of the errors linked to the backlash and the control lead to a RMS tip position error of 0.55 mm. This is suitable for the targeted application, since it is well below average abscess sizes of 41 mm reported in [4], with minimum and maximum dimensions of 8 and 105 mm, respectively.

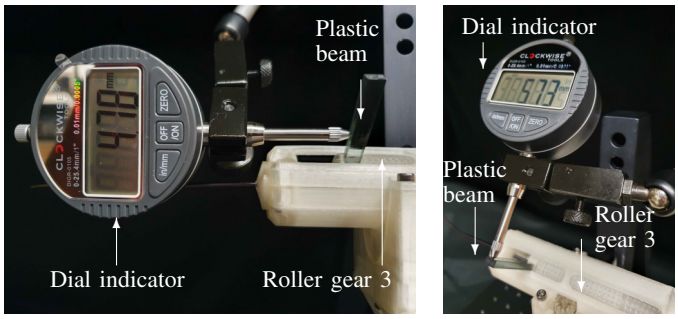

Fig. 15. Illustration of backlash measurement for the translation of roller gear 3 (T3), and (b) illustration of backlash measurement for the rotation of roller gear 3 (R3).

TABLE IV
Backlash measurement errors and standard deviations for the translation and rotation of the roller gears.

Backlash error	T3 (mm)	T2 (mm)	T1 (mm)	R3 (deg)	R2 (deg)	R1 (deg)
Mean error	0.445	0.556	0.342	3.863	4.829	4.886
Standard deviation	0.052	0.065	0.082	0.055	0.108	0.202

B. Open-loop positioning accuracy

The performance of the device is first assessed in open-loop, to evaluate its tip positioning accuracy. In this experiment, the device is grounded to focus on the evaluation of the position control algorithm without any external factors. We selected two paths that the CTR tip must follow (Fig. 16) and fabricated each using a 2 mm diameter rigid, hollow plastic

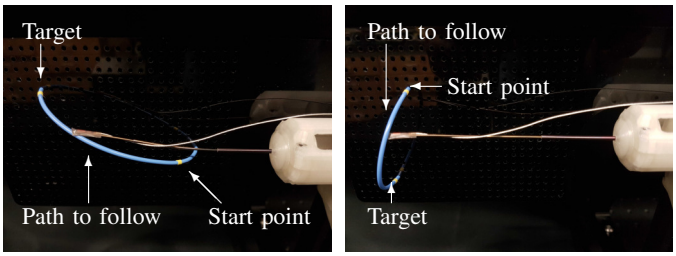

(a) (b)

Fig. 16. Path geometries used for open-loop and human-in-the-loop positioning performance assessment, including (a) path 1, and (b) path 2.

tube, with an inner diameter of 1.3 mm. Path 1 (Fig. 16(a)) was designed to simulate introducing and deploying the tip along a path to reach a target in the human body (i.e. to reach the abdominal cavity in the case of percutaneous abscess drainage for the considered application), and Path 2 (Fig. 16(b)) was designed to simulate the movement of the tip between two targets located in an area of interest (i.e. for coverage of the volume to be drained). The combination of both paths was also designed to cover a large part of the workspace of the device, to make them suitable for overall performance evaluation. The complete setup is visible in Fig. 17. Both the proposed device and the paths to follow are attached to an optical table. An electromagnetic tracking system (NDI trackSTAR, Waterloo, Canada) with a 6-DOF sensor (model 90) with an outer diameter of 0.9 mm is used to sense 3D positions, with position acquisitions every 10 ms for all the experiments.

An initial calibration is performed between the magnetic field generator and the proposed device, by sensing points of known locations on the device using the 6-DOF sensor. The location of the start and end points, visible in Fig. 16, along with the shape of each path to follow are then sensed by sliding the sensor inside the empty channel of the paths multiple times. A dense set P_{path} of $M = 10000$ is captured and averaged for error computation. A sparse path with points equally spaced 1 mm apart, P_{reach}, is extracted from the dense set P_{path}, and transformed to the device coordinate frame, for the tip to follow. The sensor is then attached to the tip of the CTR. Calibration of the CTR tube positions and orientations are then performed. For this purpose, the deployed lengths of the tubes are physically measured and iteratively adjusted to match the maximum deployed tube lengths, considered as the reference position. The tube base angles are also iteratively adjusted such that the tube assembly lies in a unique vertical plane in the device frame, using the method initially described in [42]. The CTR is then commanded to reach each point of the path in P_{reach} from its start point to its end point. This process is repeated 3 times for each path, with the same initial CTR configurations. The paths are removed from the experimental setup during this step, to avoid any physical interference with the CTR body.

The first row of Table V represents the shapes of paths 1 and 2, respectively, as well as the paths taken by the CTR tip. Tables VI and VII present tip positioning errors during deployment, computed using P_{path}, with mean error $\bar{e} = \frac{1}{N}\sum_{i=1}^{N} e_i$, standard deviation $s = \sqrt{\frac{1}{N}\sum_{i=1}^{N}(e_i - \bar{e})^2}$, and maximum error $e_{max} = \max_{i=1\cdots N}(e_i)$, with $e_i = \min_{j=1\cdots M} d(\mathbf{P}_{tip,i}, \mathbf{P}_{path,j})$, where N is the total number of points recorded during the entire CTR deployment, and d the Euclidean distance in $\mathbb{R}^3$. Deviations of the CTR tip paths to the desired ones are observed, with mean, standard deviation, and maximum errors of 2.2, 2.0, and 9.6 mm on average for path 1, and 3.3, 0.7, and 5.2 mm on average for path 2. The final tip positions are 7.2 and 6.8 mm away from the target on average for path 1 and 2, respectively. These errors, larger that the control and backlash errors combined, can be explained by phenomenons such as tube manufacturing errors, and clearance and friction between tube pairs, as recent work suggests [43], and could be lowered by using more advanced models that need to account for these phenomena. Despite these path deviations, the experiments resulted in low fluctuations of the tip paths in 3D space, illustrating good tip positioning repeatability. The latter is evaluated by computing the minimum distance between each point on a tip path and its closest neighbor on the other paths. On average, a point on any tip path is at a distance of 0.29 mm to its closest neighbor on another

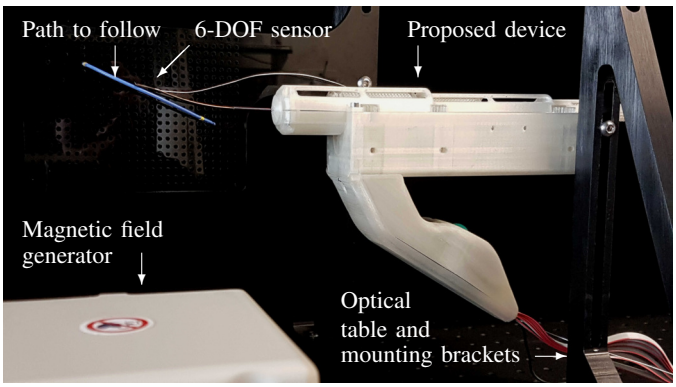

Fig. 17. Experimental setup used for the assessment of the open-loop tip positioning performance. The device and the path to follow are mounted to an optical table. An electromagnetic tracking system and a 6-DOF sensor are used to measure the CTR tip position.

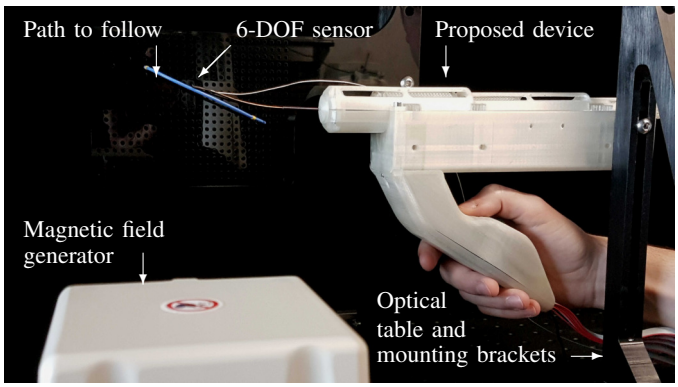

Fig. 18. Experimental setup used for the assessment of the human-in-the-loop tip positioning performance. The device and the path to follow are mounted to an optical table. An electromagnetic tracking system and a 6-DOF sensor are used to measure the CTR tip position during teleoperation.

TABLE V
PATHS TAKEN BY THE CTR TIP FOR OPEN-LOOP AND HUMAN-IN-THE-LOOP CONTROL, WHILE FOLLOWING PATHS 1 AND 2.

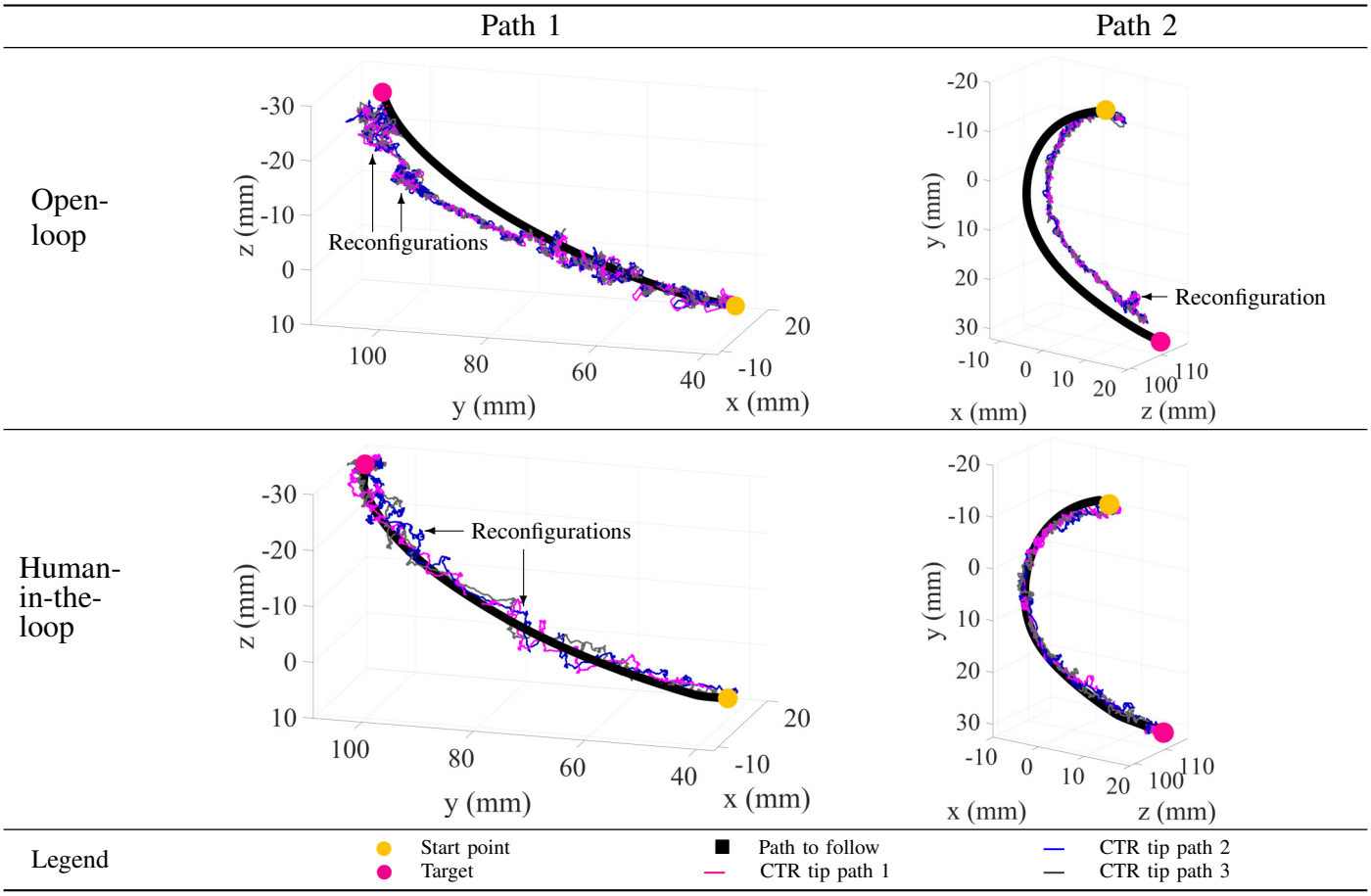

TABLE VI
PATH FOLLOWING ERROR DURING OPEN-LOOP AND HUMAN-IN-THE-LOOP CONTROL FOR PATH 1, WITH MEAN, STANDARD DEVIATION, MAXIMUM AND FINAL TIP POSITION ERRORS FOR EACH TRIAL.

	Trial number	Mean error (mm)	Std deviation (mm)	Max error (mm)	Final tip error (mm)
Open-loop	1	2.2	2.0	9.6	7.4
	2	2.2	1.9	9.9	6.9
	3	2.2	1.9	9.4	7.4
Human-in-the-loop	1	1.1	0.8	3.4	0.4
	2	1.4	0.8	3.8	1.0
	3	1.3	1.0	4.4	0.6

TABLE VII
PATH FOLLOWING ERROR DURING OPEN-LOOP AND HUMAN-IN-THE-LOOP CONTROL FOR PATH 2, WITH MEAN, STANDARD DEVIATION, MAXIMUM AND FINAL TIP POSITION ERRORS FOR EACH TRIAL.

	Trial number	Mean error (mm)	Std deviation (mm)	Max error (mm)	Final tip error (mm)
Open-loop	1	3.4	0.7	5.2	6.9
	2	3.3	0.6	5.1	6.6
	3	3.3	0.7	5.4	6.8
Human-in-the-loop	1	0.3	0.6	2.0	0.3
	2	0.4	0.6	2.3	1.3
	3	0.3	0.5	2.1	1.2

tip path for Path 1, with an RMS distance of 0.35 mm and maximum distance of 3.19 mm, and at an average distance of 0.28 mm for Path 2, with an RMS distance of 0.33 mm and maximum distance of 1.23 mm. These values are on the same order as values expected due to effects of backlash, which were shown to lead to RMS tip position errors of 0.55 mm, with a maximum error of 1.75 mm. CTR reconfigurations occurred during deployment, as labeled in the first row of Table V. Local deviations of the CTR tip are visible during reconfigurations, due to the fact that the kinematic model used does not take tube clearance and friction into account. However, they allow the robot to continue deploying along the desired path, while previous control method would have lead to infeasible tube configurations, which shows the benefits of the proposed method.

C. Human-in-the-loop positioning accuracy

We next evaluate the tip positioning accuracy in a human-in-the-loop control scheme, to compensate for the open-loop positioning errors observed in the previous section. The setup is similar to the open-loop experiment and the only difference is that the human is now operating the trackball and buttons.

This method is a more realistic use case of the device, which is intended to be teleoperated with visual feedback. An operator is asked to use the trackball and buttons to have the CTR tip follow the same paths as in the open-loop case, as illustrated in Fig. 18. Each path-following experiment is repeated 3 times, with the 6-DOF sensor attached to the CTR tip to sense its position. The paths to follow and the CTR tip paths are visible in the second row of Table V. While reconfigurations of the CTR occurred for path 1, they did not occur for path 2. They once again allow the deployment to continue, by avoiding any infeasible tube configurations that would have occurred with the previous method. Additionally, positioning errors during deployment are visible in Table VI and VII for paths 1 and 2, respectively, computed using the formula given in the case of the open-loop experiment. In order to compare these results to the open-loop experiments, the radius of the path to follow (1 mm) was subtracted from e_i, to account for the fact that the tip of the CTR cannot reach the centerline of the tube representing the path, but only its external surface. With mean, standard deviation, and maximum errors 1.3, 0.9, and 3.9 mm on average for path 1 and 0.3, 0.6, and 2.1 mm on average for path 2, respectively, the distance between the paths taken by the CTR tip and the path to follow are lower than in the open-loop case. Final tip errors are also decreased, with average values of 0.7 and 0.9 mm for path 1 and path 2, respectively. The tip positioning results obtained satisfy requirements of the targeted application and validate the proposed system.

D. Dexterity and usability

To assess the performance and benefits of the proposed system, including dexterity and usability, the device is now ungrounded and operated through its user interface (trackball and buttons) by operators. The experimental setup (Fig. 19) consists of a clear plastic box, stationary in the world frame, that has a 15 mm diameter hole in the middle of its top surface, which is used as the entry point for the device, similar to a natural orifice or incision in the human body. This box contains 5 targets, represented by white plastic spheres, intentionally placed so that they cannot all be reached with a fixed device pose, nor by any conventional rigid manual surgical tool. The surrounding environment is created using larger plastic spheres, with violet ones representing areas far from the targets, and red ones representing potential obstacles, with a close proximity to them. Two types of interactions between the operators and the device are measured: (1) interactions with the user interface to control the CTR tip position, and (2) rigid body motion of the entire device. To track the position of the device, rigid frames with reflective markers are attached to it, as visible in Fig. 20 (d). The positions of the markers are tracked by a commercial optical tracking system (NaturalPoint (OptiTrack), Corvallis, Oregon). After a brief introduction to the device, five first-time operators with no surgical experience were asked to navigate the tip of the CTR to hit each individual target, in increasing number order. A successful contact means that the tip of the device should touch the target inside the circle containing the target number, which is 16 mm in diameter. The operators were not limited by any time constraint, and could use any strategy to complete the experiment.

Fig. 21 illustrates the interactions between the operators and the device over time, where the labeled sections 1 to 5 correspond to the time periods of navigation to these targets. The time required to complete the experiment is reasonable for first-time users, with an average of 87 seconds, and minimum and maximum of 75 and 114 seconds, respectively. This represents an average of 17 seconds to snake through obstacles and reach each target.

The blue lines in Fig. 21 illustrate the instantaneous velocity

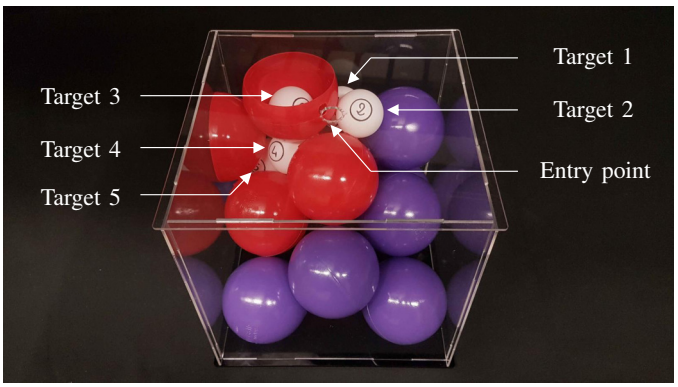

Fig. 19. Experimental setup for the preliminary user study. The targets to reach are small white plastic spheres, numbered from 1 to 5. The environment is created using larger plastic spheres, with violet ones representing areas far from the targets, and red ones representing potential obstacles.

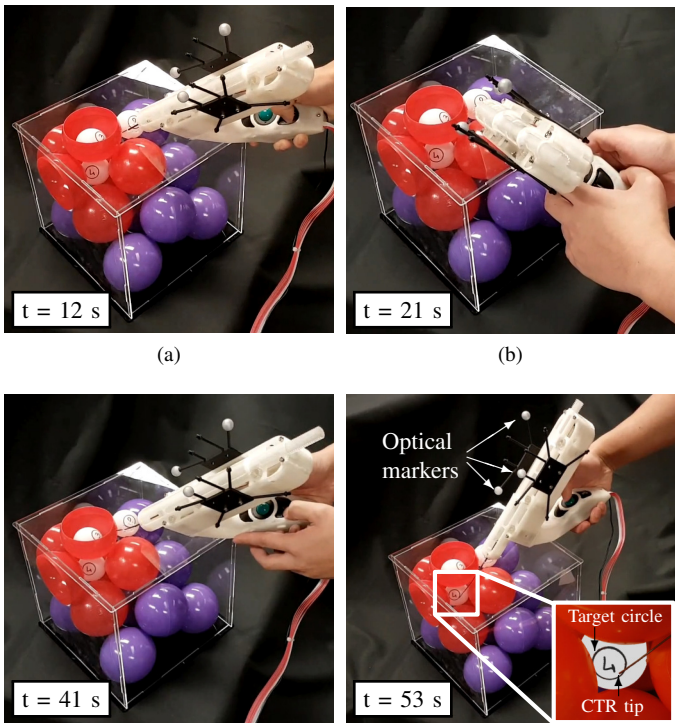

Fig. 20. Timelapse representing the pose of the device with respect to the environment of navigation for operator 2, with the images taken at (a) 12 s, (b) 21 s, (c) 41 s, and (d) 53 s. (d) contains a close-up view with the CTR tip reaching target 4.

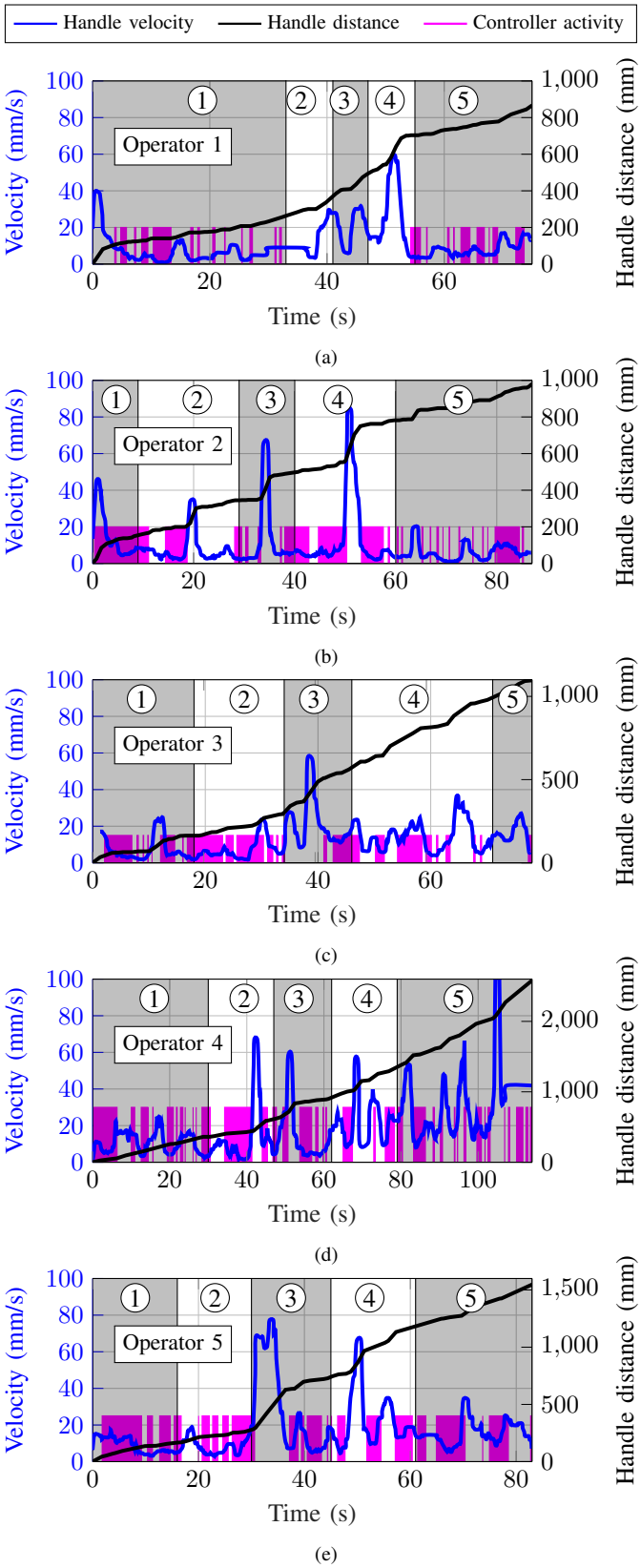

Fig. 21. Interaction between operators and the device over time while reaching targets 1 to 5, with plot (a) to (e) corresponding to operator 1 to 5. Magenta lines represent an interaction of the operator with the inputs on the device handle, while the blue lines represent the instantaneous velocity of the device handle and the black line its distance traveled by the handle over time.

of the device handle, which also represents the velocity of the operator's hand. It is computed using the locations of the markers over time with respect to the world frame, and demonstrate larger, rigid body motions of the device. Additionally, the black lines in Fig. 21 represent the distance traveled by the device handle. The magenta lines represent interactions with the control interface (i.e. the trackball and buttons). As visible in this figure, all operators use both rigid body motions and interactions with the control interface in order to reach the targets. Fig. 21 also illustrates that these two methods of movement are complementary, generally used at different times. Specifically, the control interface is not used during high velocity pose changes of the device, but rather used when the device is stationary (see all displacements of the device at velocities higher than 30 mm/s for operators 1, 2, 3 and 5 in Fig. 21 (a), (b), (c), and (e), respectively, and velocities higher than 40 mm/s for operator 4 in Fig. 21 (d)).

During these periods of time when high velocities of the device handle are measured, the device is experiencing rigid body motion leading to new poses that ease access to the targets by providing a better angle. Fig. 20 illustrates example poses of the device with respect to the environment after each important motion at high velocities for operator 2 (see provided video). These motions are a natural and straightforward way of moving the reachable workspace of the devices closer to the areas that contain targets, which may initially be out of reach. Target 5, for example, is located at a very confined location inside the environment and can only be reached with a combination of specific device angles, and specific control inputs. This shows the importance of combining both tip positioning strategies to access such confined targets. In contrast, other targets, including Target 2, can be reached either using rigid body motions of the device or using the control interface. While operators 2 to 5 used a combination of rigid body motion and control interface to navigate from Target 1 to Target 2, operator 1 only made use of rigid body motion, leading to a shorter time to reach the target (8 seconds for operator 1, compared to 20, 16, 17, and 14 seconds for operators 2 to 5, respectively). The same phenomenon is noted while reaching Targets 3 and 4, leading to higher efficiency for operator 1 compared to the others. Rigid body motion therefore appears to be an intuitive strategy and straightforward process that allows improved efficiency in several situations, and illustrates an advantage of a hand-held device, as opposed to a grounded one.

Finally, the users perceived the device to be lightweight during this user study. However, the average duration of the interaction between the operator and the device, which was 87 sec (see Fig. 21), is too short to make a conclusion about the impact of the device weight on the operator in a clinical scenario. This evaluation is left for future work, along with the assessment of operator posture and muscle fatigue potentially induced during realistic surgical procedures. In addition, the users qualitatively found the device to be rather easy to use. The main difficulties in using the device appeared to result from the presence of the workspace boundaries. While implementation of these boundaries was successful in limiting the user input to the reachable CTR workspace, they were not

easy to visualize or anticipate for the operators. In addition, the ergonomics of the user interface can be improved to enable operators to use the buttons and trackball without having to look at the device handle from time to time to localize them.

VII. Conclusion

In this paper, the first fully hand-held concentric tube robot capable of 6 DOF was presented. Its novel design enables a highly compact and lightweight system, with an overall weight of 370 g for the proposed implementation, while still allowing the use of 3 fully-actuated tubes. A control method was also introduced for tip position control of a stable CTR. It solves prior practical limitations for CTR control and includes a time-efficient way to compute and store the workspace boundaries that integrates well in the control method workflow, and allows for limits to be placed on the user input. The proposed control method was implemented on a 3-tube CTR, with computed RMS tip positioning accuracy of 0.55 mm, that can be accounted for by the inverse kinematics error as well as the backlash in the device. Operators control the robot through an interface adapted for a hand-held device. It is located on the handle and decouples the displacements of the tip to in-plane motions, using a trackball, and backward / forward motions, using buttons. The performance of the device was assessed through open-loop and human-in-the-loop experiments, with tip position accuracy that satisfies the targeted medical application, percutaneous abscess drainage, with abscess dimensions that are several orders of magnitude larger than the tip position accuracy. Finally, the interactions between the device and operators were studied through a small user study. Results showed the benefits of the proposed device, with rigid body motion used to move the reachable workspace of the device to an area of interest or to reach targets more efficiently, and with the user interface allowing navigation along curved paths and smaller tip displacements. Future work will focus on the use of tip visualization methods using medical imaging modalities such as ultrasound and CT scanners. The impact of the weight of the device on the operator in realistic medical scenarios, along with any associated effects on posture and muscle fatigue, will also be investigated.

References

[1] M. J. Mack, "Minimally Invasive and Robotic Surgery," *JAMA*, vol. 285, no. 5, pp. 568–572, 02 2001.

[2] N. Abraham, J. Young, and M. Solomon, "Meta-analysis of short-term outcomes after laparoscopic resection for colorectal cancer," *British journal of surgery*, vol. 91, no. 9, pp. 1111–1124, 2004.

[3] C. J. Payne and G.-Z. Yang, "Hand-held medical robots," *Annals of Biomedical Engineering*, vol. 42, no. 8, pp. 1594–1605, Aug 2014.

[4] D. Marin, L. M. Ho, H. Barnhart, A. M. Neville, R. R. White, and E. K. Paulson, "Percutaneous abscess drainage in patients with perforated acute appendicitis: effectiveness, safety, and prediction of outcome," *American Journal of Roentgenology*, vol. 194, no. 2, pp. 422–429, 2010.

[5] J. J. Clark and S. M. Johnson, "Laparoscopic drainage of intraabdominal abscess after appendectomy: an alternative to laparotomy in cases not amenable to percutaneous drainage," *Journal of pediatric surgery*, vol. 46, no. 7, pp. 1385–1389, 2011.

[6] K. E. Riojas, P. L. Anderson, R. A. Lathrop, S. D. Herrell, D. C. Rucker, and R. J. Webster, "A hand-held non-robotic surgical tool with a wrist and an elbow," *IEEE Transactions on Biomedical Engineering*, vol. 66, no. 11, pp. 3176–3184, Nov 2019.

[7] W. Yao, H. Elangovan, and K. Nicolaides, "Design of a flexible fetoscopy manipulation system for congenital diaphragmatic hernia," *Medical engineering & physics*, vol. 36, no. 1, pp. 32–38, 2014.

[8] P. L. Anderson, R. A. Lathrop, and R. J. Webster III, "Robot-like dexterity without computers and motors: a review of hand-held laparoscopic instruments with wrist-like tip articulation," *Expert review of medical devices*, vol. 13, no. 7, pp. 661–672, 2016.

[9] H. Yamashita, K. Matsumiya, K. Masamune, H. Liao, T. Chiba, and T. Dohi, "Two-dofs bending forceps manipulator of 3.5-mm diameter for intrauterine fetus surgery: feasibility evaluation," *International Journal of Computer Assisted Radiology and Surgery*, vol. 1, p. 218, 2006.

[10] F. Focacci, M. Piccigallo, O. Tonet, G. Megali, A. Pietrabissa, and P. Dario, "Lightweight hand-held robot for laparoscopic surgery," in *Proceedings 2007 IEEE International Conference on Robotics and Automation*, April 2007, pp. 599–604.

[11] J. Legrand, A. Javaux, M. Ourak, D. Wenmakers, T. Vercauteren, J. Deprest, S. Ourselin, K. Denis, and E. Vander Poorten, "Handheld active add-on control unit for a cable-driven flexible endoscope," *Frontiers in Robotics and AI*, vol. 6, p. 87, 2019.

[12] J. Burgner-Kahrs, D. C. Rucker, and H. Choset, "Continuum robots for medical applications: A survey," *IEEE Transactions on Robotics*, vol. 31, no. 6, pp. 1261–1280, Dec 2015.

[13] P. Sears and P. Dupont, "A steerable needle technology using curved concentric tubes," in *2006 IEEE/RSJ International Conference on Intelligent Robots and Systems*, Oct 2006, pp. 2850–2856.

[14] R. J. Webster, A. M. Okamura, and N. J. Cowan, "Toward active cannulas: Miniature snake-like surgical robots," in *2006 IEEE/RSJ international conference on intelligent robots and systems*. IEEE, 2006, pp. 2857–2863.

[15] P. E. Dupont, J. Lock, B. Itkowitz, and E. Butler, "Design and control of concentric-tube robots," *IEEE Transactions on Robotics*, vol. 26, no. 2, pp. 209–225, April 2010.

[16] J. Burgner, P. J. Swaney, R. A. Lathrop, K. D. Weaver, and R. J. Webster, "Debulking from within: a robotic steerable cannula for intracerebral hemorrhage evacuation," *IEEE Transactions on Biomedical Engineering*, vol. 60, no. 9, pp. 2567–2575, 2013.

[17] Q. Peyron, K. Rabenorosoa, N. Andreff, and P. Renaud, "A numerical framework for the stability and cardinality analysis of concentric tube robots: Introduction and application to the follow-the-leader deployment," *Mechanism and Machine Theory*, vol. 132, pp. 176 – 192, 2019.

[18] F.-Y. Lin, C. Bergeles, and G.-Z. Yang, "Biometry-based concentric tubes robot for vitreoretinal surgery," in *Engineering in Medicine and Biology Society (EMBC), 2015 37th Annual International Conference of the IEEE*. IEEE, 2015, pp. 5280–5284.

[19] P. J. Swaney, A. W. Mahoney, A. A. Remirez, E. Lamers, B. I. Hartley, R. H. Feins, R. Alterovitz, and R. J. Webster, "Tendons, concentric tubes, and a bevel tip: Three steerable robots in one transoral lung access system," in *2015 IEEE International Conference on Robotics and Automation (ICRA)*, May 2015, pp. 5378–5383.

[20] G. Dwyer, F. Chadebecq, M. T. Amo, C. Bergeles, E. Maneas, V. Pawar, E. Vander Poorten, J. Deprest, S. Ourselin, P. De Coppi, T. Vercauteren, and D. Stoyanov, "A continuum robot and control interface for surgical assist in fetoscopic interventions," *IEEE Robotics and Automation Letters*, pp. pre–print, 2017.

[21] H. Yu, L. Wu, K. Wu, and H. Ren, "Development of a multi-channel concentric tube robotic system with active vision for transnasal nasopharyngeal carcinoma procedures," *IEEE Robotics and Automation Letters*, vol. 1, no. 2, pp. 1172–1178, 2016.

[22] A. H. Gosline, N. V. Vasilyev, E. J. Butler, C. Folk, A. Cohen, R. Chen, N. Lang, P. J. Del Nido, and P. E. Dupont, "Percutaneous intracardiac beating-heart surgery using metal mems tissue approximation tools," *The International Journal of Robotics Research*, vol. 31, no. 9, pp. 1081–1093, 2012.

[23] R. J. Hendrick, C. R. Mitchell, S. D. Herrell, and R. J. Webster III, "Hand-held transendoscopic robotic manipulators: A transurethral laser prostate surgery case study," *The International journal of robotics research*, vol. 34, no. 13, pp. 1559–1572, 2015.

[24] S. Okazawa, R. Ebrahimi, R. Rohling, and S. E. Salcudean, "Hand-held steerable needle device," in *Medical Image Computing and Computer-Assisted Intervention - MICCAI 2003*, R. E. Ellis and T. M. Peters, Eds. Berlin, Heidelberg: Springer Berlin Heidelberg, 2003, pp. 223–230.

[25] M. Torabi, R. Gupta, and C. J. Walsh, "Compact robotically steerable image-guided instrument for multi-adjacent-point (map) targeting," *IEEE Transactions on Robotics*, vol. 30, no. 4, pp. 802–815, Aug 2014.

[26] M. U. Farooq, W. Y. Kim, and S. Y. Ko, "A cost-effective and miniaturized actuation system for two three-tube concentric tube robots with

parallel actuation," in *2017 17th International Conference on Control, Automation and Systems (ICCAS)*, Oct 2017, pp. 1382–1386.
[27] M. U. Farooq, B. Xu, and S. Y. Ko, "A concentric tube-based 4-dof puncturing needle with a novel miniaturized actuation system for vitrectomy," *BioMedical Engineering OnLine*, vol. 18, no. 1, p. 46, Apr 2019.
[28] S. Amack, M. Rox, J. Mitchell, T. Efe Ertop, M. Emerson, A. Kuntz, F. Maldonado, J. Akulian, J. Gafford, R. Alterovitz, and R. J. Webster III, "Design and control of a compact modular robot for transbronchial lung biopsy," vol. 10951, 2019.
[29] J. Burgner, P. J. Swaney, D. C. Rucker, H. B. Gilbert, S. T. Nill, P. T. Russell, K. D. Weaver, and R. J. Webster, "A bimanual teleoperated system for endonasal skull base surgery," in *2011 IEEE/RSJ international conference on intelligent robots and systems*. IEEE, 2011, pp. 2517–2523.
[30] C. Fellmann, D. Kashi, and J. Burgner-Kahrs, "Evaluation of input devices for teleoperation of concentric tube continuum robots for surgical tasks," in *Medical Imaging 2015: Image-Guided Procedures, Robotic Interventions, and Modeling*, vol. 9415. International Society for Optics and Photonics, 2015, p. 94151O.
[31] H. B. Gilbert, D. C. Rucker, and R. J. Webster III, *Concentric Tube Robots: The State of the Art and Future Directions*. Cham: Springer International Publishing, 2016, pp. 253–269.
[32] D. C. Rucker, I. Robert J. Webster, G. S. Chirikjian, and N. J. Cowan, "Equilibrium conformations of concentric-tube continuum robots," *The International Journal of Robotics Research*, vol. 29, no. 10, pp. 1263–1280, 2010.
[33] R. J. Hendrick, H. B. Gilbert, and R. J. Webster, "Designing snap-free concentric tube robots: A local bifurcation approach," in *2015 IEEE International Conference on Robotics and Automation (ICRA)*, May 2015, pp. 2256–2263.
[34] J. Burgner-Kahrs, H. B. Gilbert, J. Granna, P. J. Swaney, and R. J. Webster, "Workspace characterization for concentric tube continuum robots," in *2014 IEEE/RSJ International Conference on Intelligent Robots and Systems*, Sep. 2014, pp. 1269–1275.
[35] J. Granna and J. Burgner, "Characterizing the workspace of concentric tube continuum robots," in *ISR/Robotik 2014; 41st International Symposium on Robotics*, June 2014, pp. 1–7.
[36] C. Bergeles, A. H. Gosline, N. V. Vasilyev, P. J. Codd, J. Pedro, and P. E. Dupont, "Concentric tube robot design and optimization based on task and anatomical constraints," *IEEE Transactions on Robotics*, vol. 31, no. 1, pp. 67–84, 2015.
[37] F. Nigl, S. Li, J. E. Blum, and H. Lipson, "Structure-reconfiguring robots: Autonomous truss reconfiguration and manipulation," *IEEE Robotics & Automation Magazine*, vol. 20, no. 3, pp. 60–71, 2013.
[38] T. K. Morimoto, E. W. Hawkes, and A. M. Okamura, "Design of a compact actuation and control system for flexible medical robots," *IEEE Robotics and Automation Letters*, vol. 2, no. 3, pp. 1579–1585, July 2017.
[39] P. E. Dupont, J. Lock, and B. Itkowitz, "Real-time position control of concentric tube robots," *2010 IEEE International Conference on Robotics and Automation*, pp. 562–568, 2010.
[40] D. C. Rucker and R. J. Webster, "Computing jacobians and compliance matrices for externally loaded continuum robots," in *2011 IEEE International Conference on Robotics and Automation*, May 2011, pp. 945–950.
[41] R. Xu, A. Asadian, A. S. Naidu, and R. V. Patel, "Position control of concentric-tube continuum robots using a modified jacobian-based approach," in *2013 IEEE International Conference on Robotics and Automation*, May 2013, pp. 5813–5818.
[42] R. Grassmann, V. Modes, and J. Burgner-Kahrs, "Learning the forward and inverse kinematics of a 6-dof concentric tube continuum robot in se(3)," in *2018 IEEE/RSJ International Conference on Intelligent Robots and Systems (IROS)*, Oct 2018, pp. 5125–5132.
[43] J. Ha, G. Fagogenis, and P. E. Dupont, "Modeling tube clearance and bounding the effect of friction in concentric tube robot kinematics," *IEEE Transactions on Robotics*, vol. 35, no. 2, pp. 353–370, April 2019.

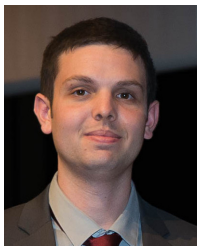

Cédric Girerd received an Engineering degree in Mechatronics from SIGMA Clermont and a Master of Science in Robotics from Univ. Blaise Pascal in Clermont-Ferrand, France, in 2014. He also received a Ph.D. degree in Robotics from the Univ. of Strasbourg, France, in 2018. He is currently working as a Postdoctoral Researcher at the University of California, San Diego. His research focuses on the design and control of continuum robots.

Tania K. Morimoto received the B.S. degree from Massachusetts Institute of Technology, Cambridge, MA, in 2012 and the M.S. and Ph.D. degrees from Stanford University, Stanford, CA, in 2015 and 2017, respectively, all in mechanical engineering. She is currently an Assistant Professor of mechanical and aerospace engineering and an Assistant Professor of surgery with University of California, San Diego. Her research interests include robotics, haptics, and engineering education.